

Seismic damage performance of the steel fiber reinforced face slab in the concrete-faced rockfill dam



Yongqian Qu^{a,b}, Degao Zou^{a,b,*}, Xianjing Kong^{a,b}, Jingmao Liu^{a,b}, Yu Zhang^{a,b}, Xiang Yu^{a,b}

^a The State Key Laboratory of Coastal and Offshore Engineering, Dalian University of Technology, Dalian, Liaoning 116024, China

^b School of Hydraulic Engineering, Dalian University of Technology, Dalian, Liaoning 116024, China

ARTICLE INFO

Keywords:

Concrete-faced rockfill dam (CFRD)
Steel fiber reinforced concrete
Plastic damage model
Generalized plasticity model

ABSTRACT

Damage and cracks in concrete face slabs threaten the safety of concrete-faced rockfill dams (CFRDs). The use of fiber-reinforced concrete is an effective engineering measure that prevents the formation of cracks in face slabs. However, there is little research regarding steel fiber reinforced CFRDs. In this study, dynamic elasto-plastic finite analyses were performed to investigate the performance of reinforced concrete (RC) and steel fiber reinforced concrete (SFRC) face slabs for a two-dimensional 250 m high CFRD. A widely used plastic damage model was modified to capture the influence of the fiber content on the behavior of concrete. Additionally, the rockfill material was described using a generalized plasticity model. The interfaces between the face slabs and the rockfill were modeled using a three-dimensional state-dependent elasto-plastic model. The damage development and equivalent crack width in RC and SFRC face slabs were investigated under varying intensities of ground motions. The results indicate that the damage to the SFRC face slab is much less than that of the RC face slab. The extent of the damage decreases by 23%, the range of damage decreases by 79%, and the maximum equivalent crack width decreases by 32%. The SFRC can greatly reduce the earthquake-induced damage to the face slab. Thus, SFRC face slabs can be used to improve the anti-seismic capabilities of CFRDs in meizoseismal areas.

1. Introduction

Concrete-faced rockfill dams (CFRDs) have become a viable dam type due to their adaptability to various environments and climates, reliability and economic nature [1,2]. To meet the increasing demand for energy, numerous high CFRDs have been built in Southwest China and located in the Himalayan seismic belt with potentially heavy seismic activity [3]. For example, the design intensities based on the China seismic intensity scale (CSIS) for the Jilintai I Dam (157 m high), Zipingpu Dam (156 m high), Longshou II Dam (146.5 m high), Jiudianxia Dam (133 m high), and Gongboxia Dam (132.2 m high) are VIII or higher [4]. Dam failures may cause catastrophic economic damage and loss of lives; therefore, the seismic safety of these high dams has received widespread attention.

Because face slabs are the main anti-seepage structures of CFRDs, their safety and reliable operation remain the major research topics of the dam engineering community [5]. However, drying shrinkage cracks and thermal contraction cracks form during face slab construction because the face slab is a massive concrete structure. For example, 235 visible cracks have been found in the Xibeikou CFRD, of which 135

cracks were wider than 0.3 mm [6]. Similarly, 355 cracks with widths greater than 0.3 mm were found in the Tianshengqiao I Dam [7], and 594 cracks formed in the Gongboxia Dam prior to impoundment, of which 199 were more than 0.2 mm wide [8]. For CFRDs that are built in seismic zones with high intensity indexes, the earthquake damage to face slabs cannot be neglected. During the Wenchuan earthquake (2008), dislocations occurred in the Phase II and III face slabs of the Zipingpu Dam; the maximum dislocation width and length were 17 cm and 340 m, respectively [9]. During the Sierra Madre earthquake (1991), cracks occurred in the concrete face slab along the dam abutments on both sides of the Cogswell CFRD; the maximum crack width was 12.7 mm [10].

Two main engineering methods are currently used for the prevention or reduction of cracks in face slabs. One solution is to increase the amount of rebar in the face slab. For example, within 5 m of the joint between the Phase I and II face slabs in the Bakun Dam, the reinforcing mesh is augmented from one layer to two layers [11]. The other solution is to use new materials in the impervious face slab. For example, steel fiber reinforced concrete (SFRC) is used in the joint between the Phase I and II face slabs of the Longshou II Dam [12], polyacrylonitrile

* Corresponding author at: The State Key Laboratory of Coastal and Offshore Engineering, Dalian University of Technology, Dalian, Liaoning 116024, China.
E-mail address: zoudegao@dlut.edu.cn (D. Zou).

(PAN) fiber reinforced concrete is used in part of the face slab of the Shuibuya Dam [13], and concrete that contains polypropylene fiber and magnesium oxide (MgO) is used in the Hongjiadu Dam [14].

Fiber reinforced concrete is a composite material that uses cement, mortar or concrete as the base material and metallic, inorganic or organic fibers as the reinforcing materials. Relative to normal concrete, fiber reinforced concrete has greater strength, crack resistance and toughness [15–17]. SFRC is one of the most widely used types of fiber reinforced concrete. The use of SFRC can greatly decrease the amount of early-stage contraction and the number of drying shrinkage cracks [18,19]. Additionally, even after the concrete has cracked, the steel fibers in the crack can still transfer loads, resulting in the formation of multiple microcracks. Under identical conditions, the total width of multiple cracks in SFRC is less than 1/10 of the total width of ordinary concrete cracks [18,19]. Yang et al. [18] and Budweg et al. [19] discussed the feasibility of SFRC without adding rebar and concluded that the use of SFRC without rebar can avoid the adverse effects of reinforcing mesh construction on cushion and sealing structures, save labor and shorten construction time. However, no studies have performed numerical analyses to investigate the seismic performance of SFRC face slabs.

This paper investigates the seismic performance of steel fiber reinforced CFRDs. To this end, the widely used plastic damage model presented by Lee and Fenves [20] was modified to capture the behavior of SFRC. The generalized plastic constitutive model for rockfill material and a three-dimensional (3D) state-dependent elasto-plastic model for the interface between the face slabs and the rockfill were employed to perform an elasto-plastic seismic response analysis of a 250 m high CFRD. The seismic damage behavior for a steel fiber reinforced CFRD and a reinforced CFRD was analyzed and compared under varying intensities of ground motions. The results provide technical approaches and references for the design and application of steel fiber reinforced CFRDs.

2. Plastic damage model for concrete

2.1. Lee-Fenves model [20]

Under high or complex stresses, normal concrete will exhibit strain softening and stiffness degradation, both of which cannot be represented by traditional linear elastic models. To reasonably describe these characteristics, Lubliner and Oller [21] proposed the Barcelona plastic damage model by combining the traditional plastic theory with the damage theory, which is clear and easy to implement numerically. By introducing the tension-compression duality to the Barcelona model, Lee and Fenves extended its applicability to effective stress space and obtained the more widely used Lee-Fenves plastic damage model [20]. The Lee-Fenves model includes the following three main parts.

2.1.1. Stress-strain relationship

The stiffness degradation variable D , which characterizes the degree of material damage, was introduced based on the incremental theory of plasticity (when $D = 0$, the material is intact; when $D = 1$, the material is completely destroyed). The stress-strain relationship for the plastic damage model for concrete can be expressed as

$$\sigma = (1 - D)\bar{\sigma} = (1 - D)E_0 : (\varepsilon - \varepsilon^p) \quad (1)$$

where $\bar{\sigma}$ is the effective stress, E_0 is the initial elastic modulus of the material, ε is the total strain, and ε^p is the plastic strain.

2.1.2. Yield criteria and flow rules

During plastic deformation, the plastic strain can be calculated by the non-associated flow rule, which is expressed as

$$\varepsilon^p = \lambda \frac{\partial \Phi(\bar{\sigma})}{\partial \bar{\sigma}}, \quad \Phi = \sqrt{2J_2} + \alpha_p I_1 \quad (2)$$

where λ is the invariant of plasticity, I_1 and J_2 are the first invariant of the principle stress and the second invariant of the deviatoric stress, respectively, and α_p is a parameter related to the shear dilation of the concrete.

Lee et al. extended the yield criterion that was introduced by Lubliner to effective stress space. The yield function, which is defined by the effective stress and damage state variable, κ , is expressed as

$$\bar{F}(\bar{\sigma}, \kappa) = \frac{1}{1 - \alpha} [\alpha I_1 + \sqrt{3J_2} + \beta(\kappa) \langle \hat{\sigma}_{max} \rangle] - c_c(\kappa) \quad (3)$$

where α and β are dimensionless parameters, $\langle \hat{\sigma}_{max} \rangle$ is the representative value of the maximum principle stress, and c is the strength parameter.

2.1.3. Damage evolution

To combine the damage characteristics and plastic deformation of concrete, the plastic strain-associated fracture energy was used to describe the damage to the concrete. To characterize the tension-compression duality, Lee and Fenves used two damage variables, κ_t and κ_c , to describe the damage to concrete under tensile and compressive stress states, respectively, which provided a convenient way to describe the evolution of concrete damage under cyclic loading. The definitions of their damage variables are as follows:

$$\kappa_N = \frac{1}{g_N} \int_0^{\varepsilon^p} \sigma_N(\varepsilon^p) d\varepsilon^p \quad (4)$$

$$g_N = \int_0^\infty \sigma_N(\varepsilon^p) d\varepsilon^p, \quad g_N = G_N/l_N \quad (5)$$

where $N \in (t, c)$, t denotes tension, c denotes compression, g_N is the fracture energy density, and σ_N represents the curve of the stress-plastic strain relationship under different stress states and is expressed by the following equation for the Lee-Fenves model:

$$\sigma_N = f_{N0} [(1 + a_N) \exp(-b_N \varepsilon^p) - a_N \exp(-2b_N \varepsilon^p)] \quad (6)$$

where f_{N0} is the initial yield stress, and a_N and b_N are constants.

The damage under tensile and compressive stress states causes stiffness degradation; however, the stiffness degradation is correlated only to the corresponding damage. The stiffness degradation is expressed as

$$D_N = 1 - \left[\frac{1}{a_N} (1 + a_N - \sqrt{1 + a_N(2 + a_N)\kappa_N}) \right]^{d_N/b_N} \quad (7)$$

To combine the effects of the stiffness degradation under tensile and compressive stresses on the total stiffness degradation of the concrete, D in Eq. (1) is defined below by incorporating the effect of the opening and closing of microcracks under cyclic loading on the stiffness:

$$D(\kappa, \bar{\sigma}) = 1 - (1 - D_c(\kappa))(1 - s(\bar{\sigma})D_t(\kappa)) \quad (8)$$

where s denotes the effect of the opening and closing of microcracks under cyclic loading on the stiffness.

2.2. Plastic damage model modified for SFRC

2.2.1. Softening behavior of SFRC

The Lee-Fenves model can be applied to both concrete and reinforced concrete (RC) [5,22–24]. However, few studies have applied this model to SFRC. The introduction of steel fibers significantly increases the toughness of SFRC. The softening regions of the stress-strain relationships of SFRC and regular concrete are significantly different (Fig. 1). Therefore, the stress-plastic strain relationship in the Lee-Fenves model Eq. (6) is not applicable to SFRC. In this paper, modifications to the stress-plastic strain relationship in the Lee-Fenves model are made based on the current stress-strain relationship of SFRC. The improved model more accurately describes the stress-strain characteristics of SFRC with different steel fiber contents.

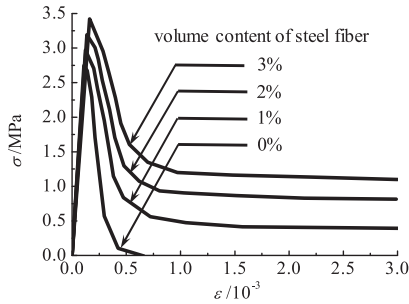


Fig. 1. Experimental stress-strain curves for tension.

This paper uses the equations that were proposed by Huang et al. [16] to describe the softening behavior of SFRC under pure tensile stress:

$$Y = \frac{X}{\alpha_f(X-1)^{1.7} + X}, \quad \alpha_f = \frac{\alpha_0}{1 + 3.58l_f\rho_f/d_f} \quad (9)$$

where Y is the stress ratio, $Y = \sigma/f_{ft}$, f_{ft} is the tensile strength, X is the strain ratio ($X \geq 1.0$ for the descending region), $X = \epsilon/\epsilon_0$, $\epsilon_0 = f_{ft}/E$, E is the elastic modulus, α_0 is the coefficient of the matrix concrete, $\alpha_0 = 0.312f_{mt}^2$, f_{mt} is the bending strength of the matrix concrete (MPa), α_f is the coefficient of the SFRC, l_f is the length of the steel fibers, d_f is the diameter of the steel fibers, and ρ_f is the volume fraction of the steel fibers. The tensile strength of SFRC, f_{ft} , can be calculated using the following equation:

$$f_{ft} = f_t \left(1 + \alpha_t \frac{l_f}{d_f} \rho_f \right) \quad (10)$$

where f_{ft} and f_t are the tensile strengths of the SFRC and the matrix concrete, respectively, and α_t is a coefficient that represents the influence of the steel fiber on the concrete and is related mainly to the types and shapes of steel fiber and the strength of the matrix concrete.

The stress-strain relationship of SFRC, $\sigma = f(\epsilon)$, can be obtained from Eq. (15). Because the stress-plastic strain relationship is required for the Lee-Fenves model, it is imperative to incorporate the plastic strain into Eq. (9) to obtain the stress-plastic strain relationship for SFRC. Several studies [25,26] have shown that when the matrix concrete of SFRC cracks, the steel fibers still play a significant role in connecting the cracked concrete; as a result, the total stiffness of SFRC does not significantly degrade. Therefore, there is an assumption that under cyclic loading, the unloading/reloading stiffness of SFRC is the same as the original stiffness, i.e., the effect of the inner damage of concrete on the total stiffness is not considered, and the variable d_N is zero. Based on this assumption, Eq. (9) can be modified, and the

following relationship can be obtained to analyze the plastic damage of SFRC:

$$\sigma = f(\epsilon); \quad \epsilon^p = \epsilon - \sigma/E_0 \quad (11)$$

2.2.2. Verification of the modified plastic damage model

To verify the validity of the modified plastic damage model and the accuracy of this model for simulating the behavior of SFRC, the constitutive relations of SFRC are simulated under uniaxial monotonic tension for several steel fiber contents. The following values are used for the various material parameters in the plastic damage model for SFRC: the elastic modulus (E) is 31.0 GPa, the Poisson ratio (ν) is 0.18, the density (ρ) is 2450 kg/m³, and the compressive strength (f_{co}) is 35.0 MPa. When the steel fiber content is 80 kg/m³, the tensile strength (f_t) is 2.95 MPa, and the corresponding fracture energy G_t is 2000 N/m; when the steel fiber content is 160 kg/m³, the tensile strength (f_t) is 3.25 MPa, the corresponding fracture energy G_t is 2400 N/m, the unit length l_c is 1.0 m, and α_p is 0.2. The fracture energy is obtained from Eq. (5). Fig. 2(a) and (b) show the experimental and simulated results of the uniaxial monotonic tensile stress [27] for SFRC with a steel content of 80 kg/m³ and 160 kg/m³, respectively. As expected, the simulated results agreed very well with the experimental results.

The constitutive relation is also simulated under uniaxial monotonic compression for SFRC with a steel fiber content of 60 kg/m³. The following numerical values are used for the various material parameters of SFRC: the elastic modulus (E) is 31.5 GPa, the Poisson ratio (ν) is 0.18, the density (ρ) is 2450 kg/m³, the compressive strength (f_{co}) is 37.0 MPa, the unit length l_c is 1.0 m, and α_p is 0.2. Fig. 2(c) shows the experimental and simulated results of the uniaxial monotonic compressive stress [28] for SFRC. As expected, the simulation results agree very well with the experimental results.

3. CFRD model and computational parameters

3.1. Finite element model

The emphasis of this paper is to investigate and compare the anti-seismic performance of RC and SFRC face slabs in CFRD during earthquake in term of tensile damage. The statistical result of a series of 3D simulations indicates that the primary tensile stress in face slab during earthquake is along the slope direction and the overstressed area is distributed in the upper central slab [29]. The seismic tensile damage to face slab from 2D analysis [5] shows a good agreement to the result of 3D simulation. The 2D simulation could describe the characteristics of tensile stress and has been frequently recognized and used to investigate CFRDs [5,30–33].

This study uses a computational model for a 2D CFRD with the

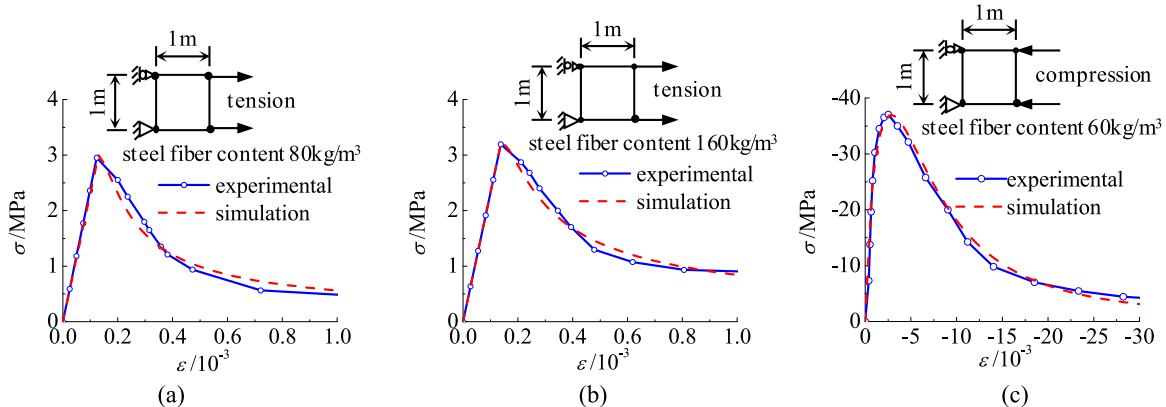


Fig. 2. Stress-strain relationship of steel fiber reinforced concrete under monotonic loading.

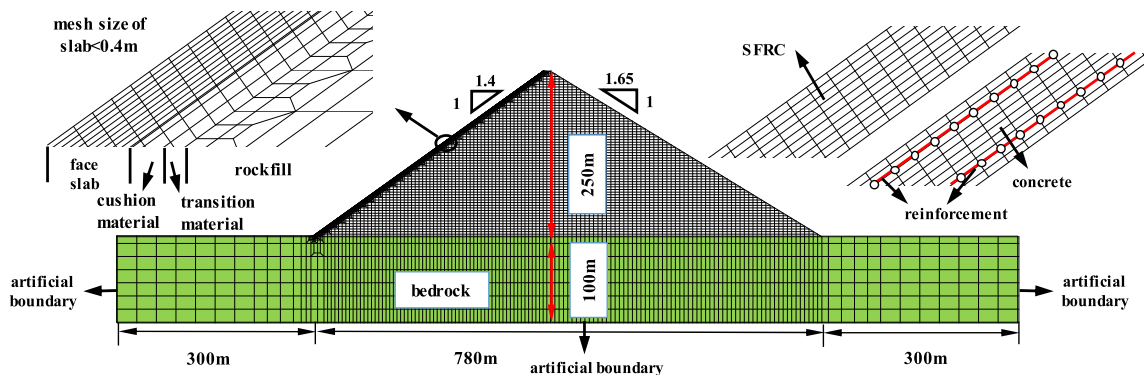


Fig. 3. Finite element model of two dimensional CFRD. (a) horizontal component in river direction (b) Vertical component.

following assumptions. The dam has a height of 250 m with an upstream dam slope ratio of 1:1.4 and a downstream dam slope ratio of 1:1.65. The depth and width of the foundation are 100 m and 1380 m, respectively. The thicknesses of the face slab are determined according to the “Design Code for Concrete Face Rockfill Dams.” The face slab is 0.3 m thick at the top of the dam, and the thickness at each location on the dam is determined by $t = 0.3 + 0.0035 h$, where t is the thickness of the face slab and h is the distance between the cross section and the top of the dam. Therefore, the face slab is 1.175 m thick at the bottom of the dam.

Fig. 3 shows the finite element mesh of the CFRD. The mesh of the face slab is divided into 10 layers along the thickness direction, and the mesh size of the slab is less than 0.4 m in the slope direction. The bi-directional reinforcement ratio of the face slab of the RC is 1.4% (equivalent to a steel content of 110 kg/m³). The steel mesh has a two-layer arrangement and is simulated using 2-node truss elements. The concrete and the SFRC are simulated using quadrilateral isoparametric elements. The interface elements by Goodman are used for the interface between the face slab and the cushion layers.

In the simulation, plane strain is assumed. The dam is filled with 64 layers, and the reservoir is impounded to a height of 240 m in 24 steps. Prior to seismic loading, the dam is subjected to static loading, including self-weight and hydrostatic pressure. In the dynamic calculations, an incompressible reservoir is assumed, and the hydrodynamic pressure of the face slab is simulated using the added mass method [34].

3.2. Material parameters

In this study, a generalized plasticity model is used to simulate the rockfill, a generalized plastic interface model is used to describe the interfaces between the face slabs and the rockfill, and a plastic damage model is used to simulate the regular concrete and SFRC. A detailed introduction of the generalized plasticity model is provided in the Appendix A.

The parameters of the generalized plasticity model for rockfill [35] are summarized in Table 1, and the material parameters of the interface between the face slab and the cushion layers [36] are summarized in Table 2. The steel rebar is simulated by an ideal elasto-plastic model with elastic modulus $E = 200$ GPa and yield strength $f_y = 400$ MPa. A linear elastic model is used for the overlaying bedrock of the dam body,

Table 1
Parameters of the generalized plastic model for rockfill materials.

G_0	K_0	M_g	M_f	α_f	α_g	H_0	H_{U0}	m_s
1000	1400	1.8	1.38	0.45	0.4	1800	3000	0.5
m_v	m_l	m_u	r_d	γ_{DM}	γ_u	β_0	β_1	
0.5	0.2	0.2	180	50	4	35	0.022	

Table 2
Parameters of the generalized plastic interface model.

D_{s0}/kPa	D_{n0}/kPa	M_c	e_r	λ	$a/\text{kPa}^{0.5}$	b	c
1000	1500	0.88	0.4	0.091	224	0.06	3.0
a	r_d	k_m	M_f	k	H_0/kPa	f_h	t/m
0.65	0.2	0.6	0.65	0.5	8500	2	0.1

Table 3
Parameters of the plastic damage model for reinforced concrete.

$\rho/\text{kg/m}^3$	E/GPa	ν	f_t/MPa	f_c/MPa	steel content $/\text{kg/m}^3$	l_c/m	$G_r/\text{N m}^{-1}$
2450	31	0.167	3.48	27.6	110	0.38	325

Table 4
Parameters of the plastic damage model for steel fiber reinforced concrete.

$\rho/\text{kg/m}^3$	E/GPa	ν	f_t/MPa	f_c/MPa	steel content $/\text{kg/m}^3$	l_c/m	$G_r/\text{N m}^{-1}$
2450	31	0.167	5.40	30.0	110	0.38	5000

which has a density $\rho = 2600 \text{ kg/m}^3$, an elastic modulus $E = 10 \text{ GPa}$, and a Poisson ratio $\nu = 0.25$.

The parameters of the plastic damage model for the concrete [5] and SFRC are summarized in Tables 3 and 4, respectively. The elastic modulus and Poisson ratio of SFRC are the same as those of the matrix concrete [15,16], and the compressive strength (f_c) is 10% higher than that of the matrix concrete [15–17].

3.3. Ground motion input

The ground motion input uses the simulated earthquake wave specified by the “Specifications for seismic design of hydraulic structures” (DL-5073-2000). The peak acceleration of the earthquake in the direction of the river is 0.3 g, while the peak vertical acceleration is 2/3 of the peak acceleration along the river. The acceleration time of the seismic wave is shown in Fig. 4. The duration of the seismic wave is 25.00 s, and the time step for the calculation (Δt) is 0.005 s. The input ground motion is achieved using a viscoelastic boundary and an equivalent load to simulate the interaction between the dam and the bedrock. The equivalent load can be calculated using the following equation [37]:

$$\mathbf{F}_b = \mathbf{R}_b^{\text{ef}} + \mathbf{C}_b \dot{\mathbf{u}}_b^{\text{ef}} + \mathbf{K}_b \mathbf{u}_b^{\text{ef}} \quad (12)$$

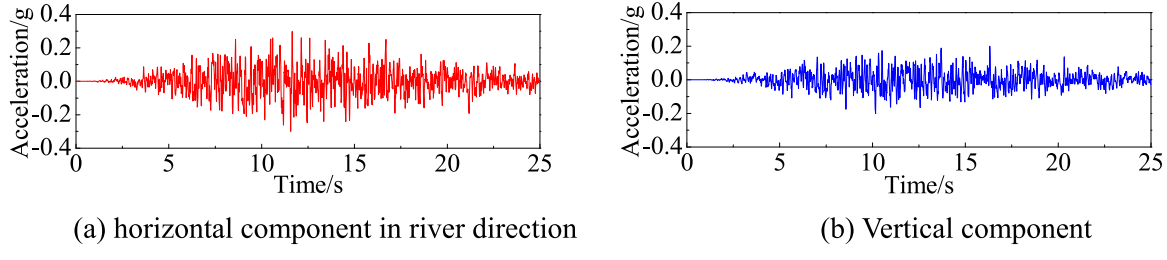


Fig. 4. Input ground motion acceleration time history.

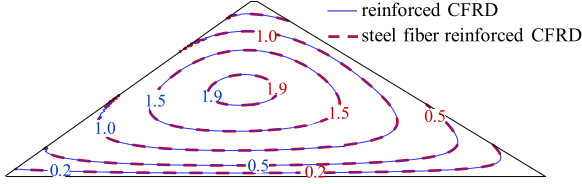


Fig. 5. The vertical settlements of the dam due to incremental dam construction and filling of reservoir (m).

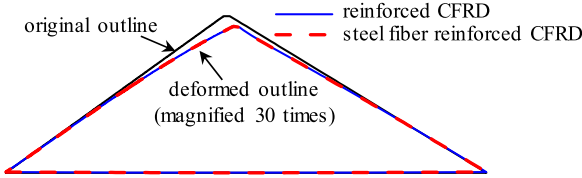


Fig. 6. The earthquake-induced additional plastic deformations of the dam body. (a) the internal forces (b) the stresses along the slope direction.

where \mathbf{u}_b^{ef} , $\dot{\mathbf{u}}_b^{ef}$ and \mathbf{R}_b^{ef} are the displacement vector, velocity vector and the corresponding force vector induced at the system boundary nodes by the free wave field, respectively, and \mathbf{K}_b and \mathbf{C}_b are the additional stiffness matrix and damping matrix of the boundary element caused by the viscoelastic artificial boundary, respectively. As shown in Fig. 4, the viscoelastic boundaries are applied along the lateral and bottom sides of the foundation.

4. Results

4.1. Dam deformation

Fig. 5 shows the vertical settlements of the dam due to incremental dam construction and reservoir impoundment for the reinforced CFRD and the steel fiber reinforced CFRD. The earthquake-induced additional plastic deformations of the dam for the two types of CFRDs are illustrated in Fig. 6. The dam deformation is consistent with the general deformation laws [38]. The face slab accounts for a very small portion of the entire dam. Therefore, the difference in the face slab materials has little effect on the stiffness and mass of the dam. The response of the dam is influenced mainly by the properties of the rockfill. As a result, the difference in the face slab materials has almost no effect on the deformation of the dam.

4.2. Face slab stress

The distribution of the internal forces and stress along the slope direction of the SFRC and RC face slabs at full-storage stage are plotted in Fig. 7 (the thickness of the face slab is magnified 30 times). The results of the two types of face slabs are consistent with the general laws [38,39]. As shown in Fig. 7, the bending moment of the face slab is well defined near the bottom, and the maximum value is 1.6×10^3 kN m. The axial force is compressive (negative) over the entire face slab and reaches a maximum (1.4×10^4 kN) of approximately $0.2 H$ (H is the dam height). The compressive stress induced by the axial force is larger than the tensile stress caused by bending (Fig. 7(b)). Therefore, the face slab is in a compressive stress state, and the compressive stress reaches

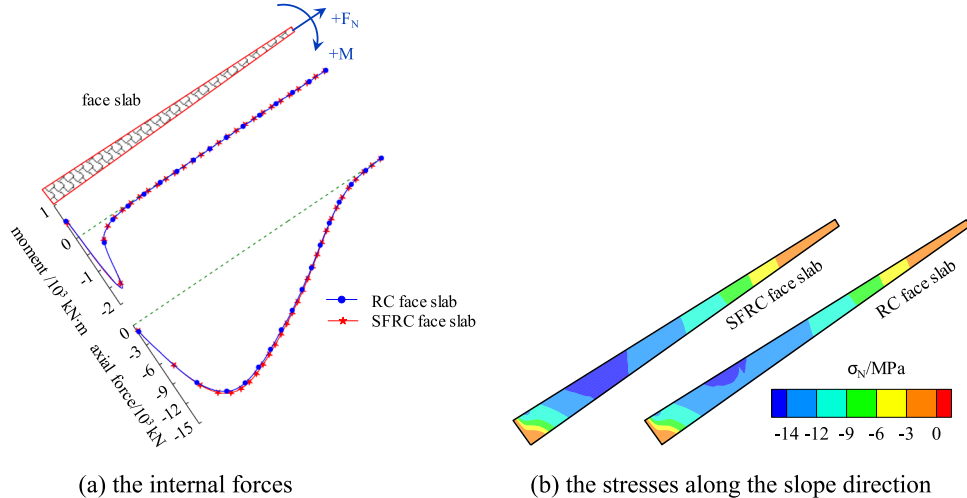


Fig. 7. The internal forces and stresses along the slope direction of the face slabs at full-storage stage. (a) the maximum internal forces (b) the minimum internal forces (c) the maximum stress along the slope direction (d) the minimum stress along the slope direction.

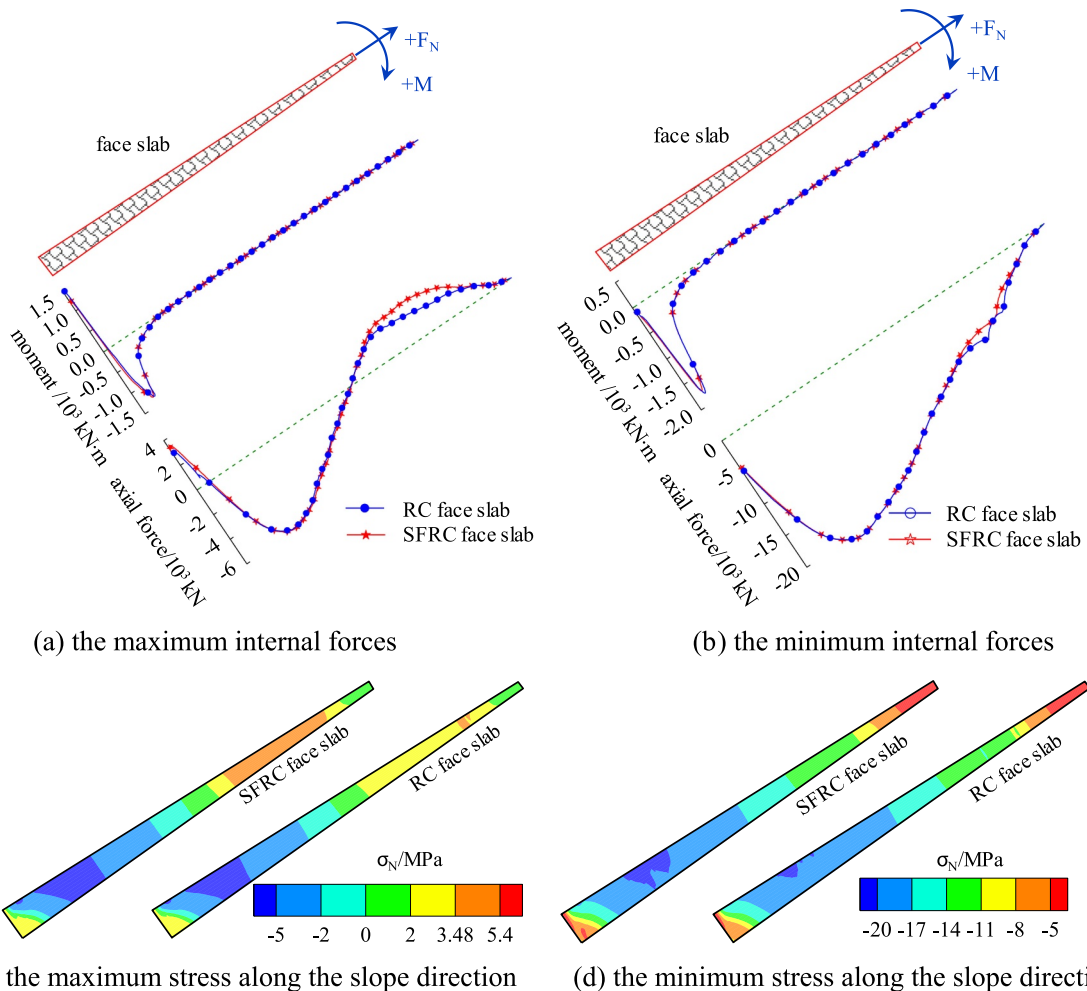


Fig. 8. The envelopes of internal forces and stress along the slope direction of the face slabs during earthquake (including static response). (a) RC face slab (b) SFRC face slab.

a maximum where the negative axial force is largest. The maximum compressive stress (approximately 14 MPa) is less than the compressive strength of concrete, and the face slab is in the elastic state at the full-storage stage. Moreover, the magnitude of the compressive stress at the bottom of the face slab gradually decreases (close to zero) from upstream to downstream due to the negative bending moment.

The envelopes (including the static response) of internal forces and stresses along the slope direction of the two types of face slabs during an earthquake are summarized in Fig. 8. The bending moment is determined mainly by the static results, i.e., the earthquake-induced additional bending moment is relatively small. The minimum axial force is

compressive (negative) over the entire face slab, and the maximum compressive stress along the slope direction (approximately 20 MPa) is less than the compressive strength of concrete. As shown in Fig. 9, the two types of face slabs are damaged (tensile) above 2/3 of the dam height. In this region, the bending is negligible; thus, the axial force is the major cause of the damage. Due to higher tensile resistance, the maximum axial force of the SFRC face slab is larger than that of the RC face slab in the damaged region. The stress is released and redistributed, and the stiffness decreases after damage occurs; therefore, the minimum axial force is also different in this region.

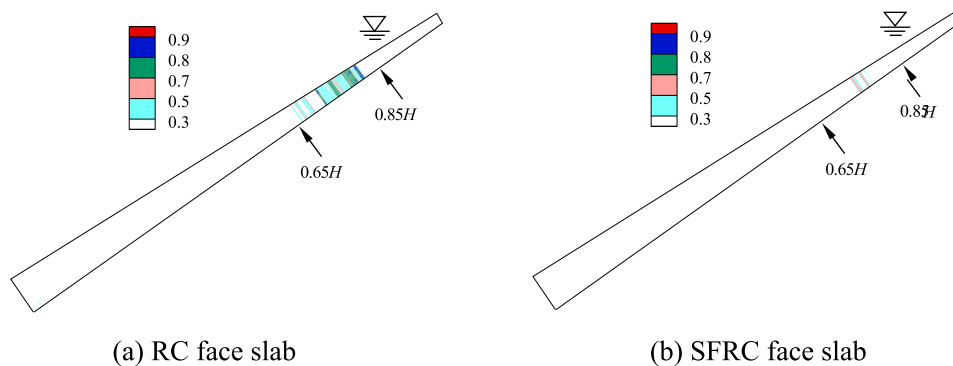


Fig. 9. The damage distribution of the face slabs at the end of earthquake.

4.3. Damage and cracks of face slabs

4.3.1. Development of damage

The seismic tensile damage to the RC face slab and the SFRC face slab after the earthquake is presented in Fig. 9 (the thickness of the face slab is magnified 30 times). Fig. 10 shows the process and development of face slab damage between $0.65 H$ and $0.85 H$ (H is the dam height). The damaged regions are almost the same in both face slabs and occur at above $2/3$ of the dam height. The damage factor of the RC face slab is greater than 0.8 and up to 0.9 in certain areas, and the damage extends for a length of 28.6 m. In contrast, the damage factor of the SFRC face slab is less than 0.7, and the damage extends for a length of 6.0 m. In

the SFRC face slab, the damage factor is 0.2 less than that in the RC face slab, and the area of damage is 79% less (Fig. 10(i)).

During the earthquake, damage occurred in the RC face slab and the SFRC face slab at $t = 9.890$ s and $t = 9.970$ s, respectively. In both slabs, the damage occurred in the region above $0.65 H$ (Fig. 10(a) and (b)). During the period of highest seismic intensity ($t = 9.890\text{--}15.460$ s), the extent of damage to the face slab gradually increased, and the location of the damage gradually moved upward (Fig. 10(h)). After the face slab was damaged and cracked, the stiffness and strength of the materials were reduced to nearly zero. As a result, the stress in the face slab was released and redistributed. Therefore, in the later period of the earthquake when the ground motion intensity

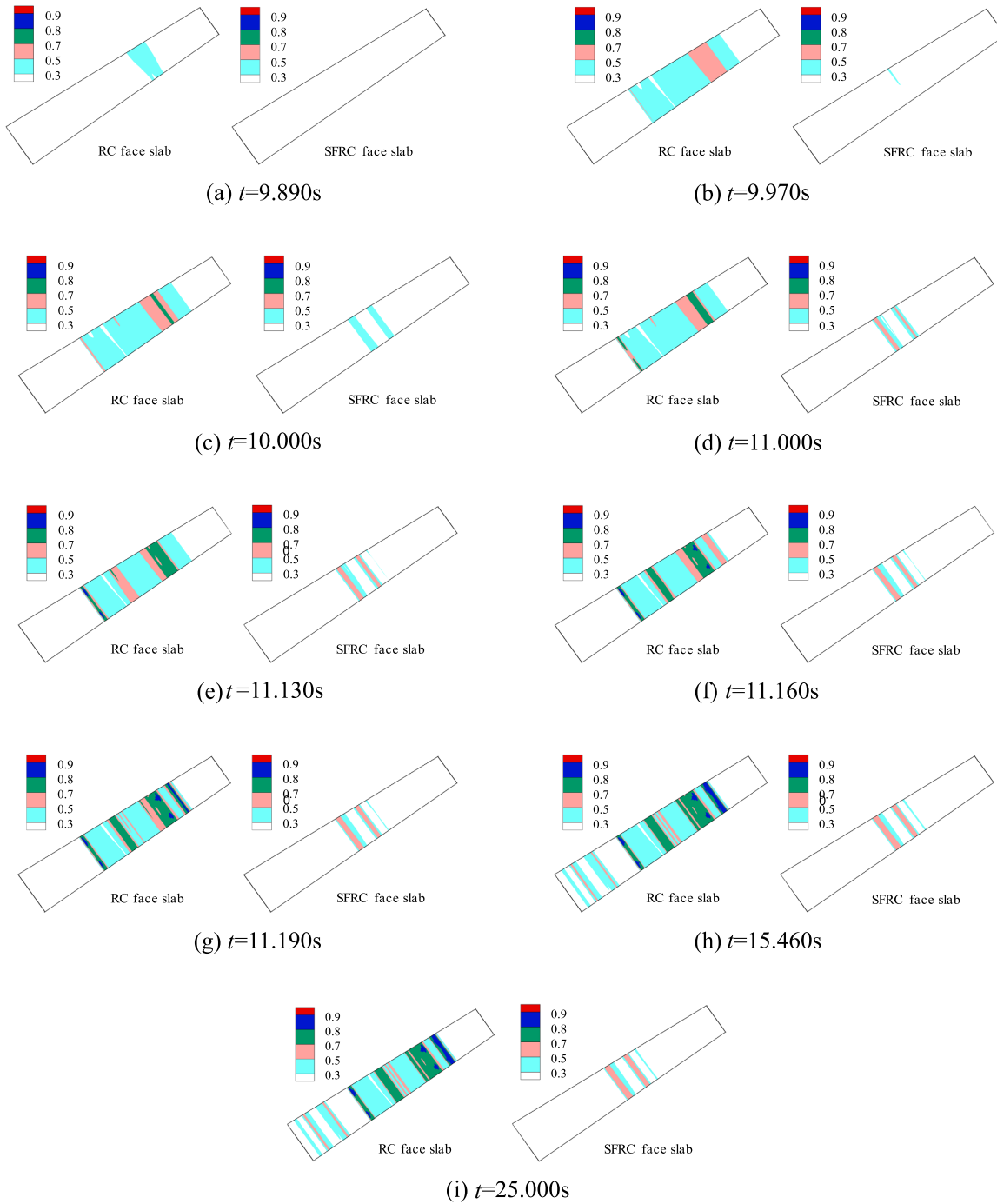


Fig. 10. The occurrence and development of damage to the face slabs at different moment from $0.65 H$ to $0.85 H$.

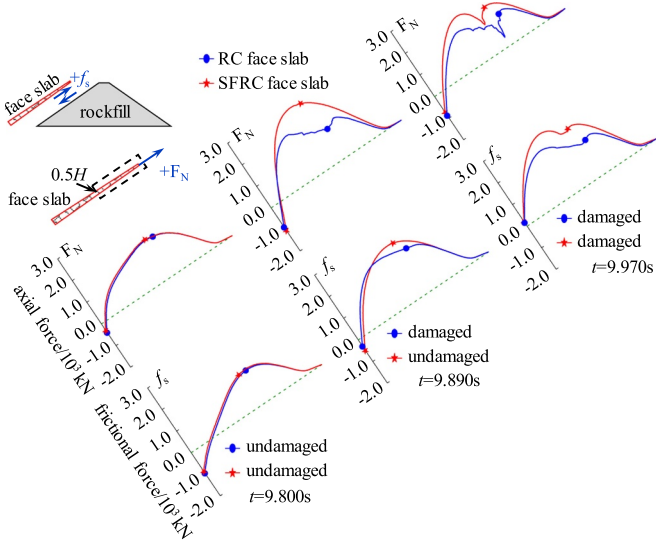


Fig. 11. The axial forces of face slabs and frictional forces between the rockfill and face slabs above 1/2 of the dam height in three typical moments. (a) RC face slab (b) SFRC face slab.

was lower, the damage to the face slab did not increase. The tensile strength of SFRC is higher than that of RC. As a result, the damage to the SFRC face slab was delayed (Fig. 10(a) and (b)).

The axial forces of the two types of face slabs and the frictional forces (accumulated shear stress in the interface) between the rockfill and face slabs above 1/2 of the dam height for typical moments during an earthquake are shown in Fig. 11. The axial forces of the RC and SFRC face slabs exhibit nearly the same values before damage occurs ($t = 9.800\text{ s}$) due to the similar elastic modulus of the concrete and steel fiber concrete material. The RC face slab is damaged at $t = 9.890\text{ s}$; the axial force is reduced for stiffness degradation and stress redistribution. The SFRC face slab is undamaged for higher tensile strength. Therefore, the axial force is larger than that in the RC face slab. The SFRC face slab is damaged at $t = 9.970\text{ s}$, and the axial force is reduced; however, this force is still larger than that in the RC face slab with higher toughness.

The distribution of the frictional force between the rockfill and face slabs is similar to the axial force, and the maximum ($1.45 \times 10^3\text{ kN}$) is approximately 88% of the maximum axial force ($1.65 \times 10^3\text{ kN}$). The frictional force is the major determinant of the axial force in the face slab. Therefore, the seismic tensile damage to the face slab can be reduced by decreasing the frictional force between the rockfill and face slabs.

Fig. 10(i) indicates that the distribution of damage to the two types of face slabs and SFRC faces are different along the thickness direction.

The maximum damage factor occurs locally on the two sides of the rebar mesh in the RC slab due to the stress concentration in the interconnecting region between the rebar and the concrete after the face slab suffered cracks and damage. However, the steel fibers are randomly dispersed and uniformly distributed in the matrix concrete, which results in a strong connection between the steel fibers and concrete. Thus, the damage in the SFRC face slab is evenly distributed over small regions with low degrees of damage.

4.3.2. Crack width

The plastic damage model cannot be used to calculate the crack width; therefore, the equivalent crack width is used to estimate the earthquake-induced cracking of the concrete face slab. Assuming that the cracks are evenly distributed along the normal direction of the cracks in each unit, the equivalent crack width, w , can be calculated using the following equation:

$$w = h\varepsilon^p \quad (13)$$

where ε^p is the plastic strain and h is the width of the crack band. Peter H. Bischoff [40] investigated the relationship between the crack band width of SFRC and that of plain concrete and obtained the following equation:

$$\frac{h_{SFRC}}{h_{plain}} = \frac{P_{cr} - P_f}{P_{cr}} \quad (14)$$

where P_{cr} is the concrete cracking force and P_f represents the tensile capacity of the fiber concrete at a crack. In the region of damage and cracks in adjacent units, the equivalent crack width represents the sum of the equivalent crack widths of those units in the normal direction of the cracks:

$$w = \sum w_i = \sum h_i \varepsilon_i^p \quad (15)$$

where h_i is the width of the crack band in the i th unit and ε_i^p is the plastic strain in the i th unit. The equivalent crack is located in the unit that contains the maximum crack strain, and the direction is the same as that normal to the crack band.

Fig. 12 shows the crack distributions in the two types of face slabs. Figs. 9 and 11 show that the location of the maximum equivalent crack is consistent with that of the damage in the face slab. The maximum equivalent crack widths in the RC face slab and the SFRC face slab are 6.88 mm and 4.71 mm, respectively. The maximum equivalent crack width is 32% smaller in the SFRC face slab than in the RC face slab. The incorporation of steel fiber into the concrete increases the tensile strength and significantly improves the toughness. A satisfactory connection is found between the steel fibers and the concrete, both of which can bear the load together and decrease the crack width in the SFRC face slab.

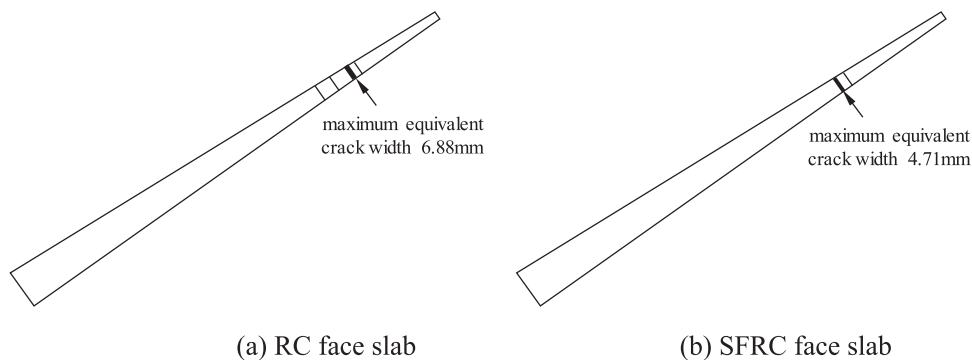


Fig. 12. The equivalent crack distribution of the face slabs at the end of earthquake. (a) RC face slab (b) SFRC face slab.

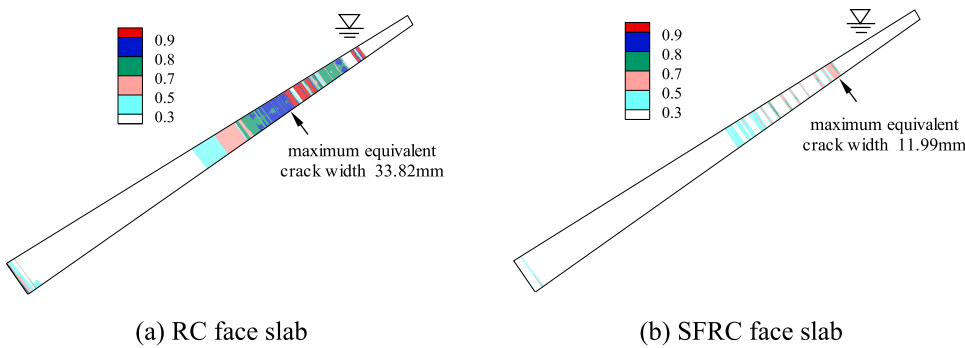


Fig. 13. The damage and equivalent crack distribution of the face slabs (the peak ground motion acceleration is 0.5 g).

Table 5

The seismic responses and the increments for the two slab types in different intensity of ground motions.

Types of face slab	Damage factor		Damage range/m			Maximum equivalent damage width/mm		
	0.3 g	0.5 g	0.3 g	0.5 g	Increment	0.3 g	0.5 g	Increment
RC face slab	0.90	0.95	28.6	101.0	72.4	6.88	33.82	26.94
SFRC face slab	0.70	0.80	6.0	31.5	25.5	4.71	11.99	7.28

4.3.3. Effect of ground motion intensity

Fig. 13 shows the distribution of damage and equivalent cracks for the two different types of face slabs when the ground motion peak acceleration is 0.5 g. Table 5 summarizes the dynamic seismic responses and the increments of the dynamic seismic responses due to the increments of the peak ground motion acceleration for the two slab types. When the peak ground motion acceleration increases to 0.5 g, the damage factor of the RC face slab is 0.9 and exceeds 0.95 in some zones, the damage extends for a length of 101.0 m, and the maximum equivalent crack width is 33.82 mm. In contrast, the damage factor of the SFRC face slab is less than 0.8, the damage extends for a length of 31.5 m, and the maximum equivalent crack width is 11.99 mm. The damage factor of the SFRC face slab is less than 0.15 that of the RC face slab, and the area of damage and the maximum equivalent crack width are 69% and 65% smaller, respectively. At the higher ground motion intensity, the distributions of damage are approximately the same in both face slab types, while the extent and area of the damage and maximum crack width are both higher. However, the increase in the extent of damage to the SFRC face slab is relatively small (Table 5). Therefore, for CFRDs in highly seismic regions, the SFRC face slab has better seismic performance.

5. Discussion and conclusions

The plastic damage model presented by Lee and Feveins is modified to capture the behavior of SFRC. The modified model is validated against published tests of SFRC with different steel fiber content. The generalized plastic constitutive model is employed to simulate the nonlinear behavior of rockfill materials. The interfaces between the face slabs and rockfill are modeled by a 3D state-dependent elasto-plastic model. The seismic damage behaviors for a steel fiber reinforced CFRD and a reinforced CFRD are analyzed and compared. Furthermore, the effects of the ground motion intensity are investigated.

- (1) The regions of seismic damage are approximately the same in the RC face slab and the SFRC face slab, and the damage to both occurs above 2/3 of the dam height under a medium earthquake. Seismic

damage occurs first in the regions above 65% of the face slab height, and the damage gradually moves upward to 85% of the face slab height with increasing seismic intensity.

- (2) The damage to the SFRC face slab is much less than that to the RC face slab; the extent of damage decreases by 23%, the range of damage decreases by 79%, and the maximum equivalent crack width decreases by 32%. The steel fibers are randomly and evenly distributed in the concrete, which results in a strong connection between the steel fiber and concrete so that they can bear the loads together. The incorporation of steel fiber significantly improves the concrete toughness; therefore, the SFRC face slab exhibits better seismic performance.
- (3) With increasing ground motion intensity, the extent and range of damage and the equivalent crack width all increase in both face slabs. However, the increment of the damage and cracks in the SFRC face slab are clearly smaller. The advantages of the seismic performance of the SFRC face slab are more pronounced for high CFRDs that are built in locations with high seismicity and a high potential for earthquakes.

This study was conducted under 2D plane strain conditions; vertical joints, 3D effects, and earthquakes along the dam axial direction are not considered. However, this configuration does not affect the conclusion that the SFRC face slab exhibits better seismic performance than the RC face slab. For the practical applications, the 3D numerical analysis is necessary to investigate the comprehensive characteristics of the SFRC face slab.

Acknowledgments

This work was supported by the National Key R&D Program of China (Grant no. 2017YFC0404900), the National Natural Science Foundation of China (Grant nos. 51779034 and 51608095), the Fundamental Research Funds for the Central Universities (Grant no. DUT17ZD219) and the China Postdoctoral Science Foundation (Grant no. 2018M631790).

Appendix A

Generalized plasticity model for rockfill and generalized plastic interface model

The Pastor-Zienkiewicz model was developed by Pastor and Zienkiewicz [41,42] based on the basic framework of generalized plastic mechanics. This model is applicable to not only the construction of civil engineering structures but also seismic response analyses and the direct calculation of earthquake-induced permanent deformation. In this study, the modified generalized plasticity model by the authors [38] is used for the rockfill materials. The authors modified the shear modulus G , volume modulus K , load modulus H_L , and unload modulus H_U of this model.

$$G = G_0 p_a (p/p_a)^{m_s} \quad (A1)$$

$$K = K_0 p_a (p/p_a)^{m_v} \quad (A2)$$

$$H_L = H_0 \cdot p_a \cdot (p/p_a)^{m_l} \cdot H_f \cdot (H_v + H_s) \cdot H_{DM} \cdot H_{den} \quad (A3)$$

$$H_u = \begin{cases} H_{u0} p_a (p/p_a)^{m_u} (\eta_u/M_g)^{-\gamma_u} & |\eta_u/M_g| < 1 \\ H_{u0} & |\eta_u/M_g| \geq 1 \end{cases} \quad (A4)$$

$$H_{DM} = \exp((1 - \eta/\eta_{max})\gamma_{DM}) \quad (A5)$$

$$H_{den} = \exp(\gamma d\varepsilon_v) \quad (A6)$$

where H_0 is the coefficient of the plastic modulus, H_f , H_v and H_s are the plastic coefficients, p_a is atmospheric pressure, and η_{max} is the ratio of the maximum historical stress. The modified model can better describe the stress correlation and cyclic hysteresis characteristics and has been successfully used to calculate the static and dynamic response of rockfill dams [38,43,44].

With the development of the elasto-plastic finite element analysis of CFRD, the traditional Duncan-Clough hyperbolic and ideal elasto-plastic contact surface model have been unable to meet the needs of the elasto-plastic response analysis of rockfill dams under seismic loads. Based on the framework of the generalized plasticity model and the 2D interface model [45,46] proposed by Liu et al., Liu et al. developed a 3D interface model [47] by combining the theory of the bounding surface model with state-dependent theory. In this model, a group of parameters can be used to accurately reflect the deformation characteristics of the interface under monotonous and cyclic loading in three dimensions, including shear dilation, shear contraction, hardening, softening and particle breakage.

References

- [1] Chen HQ, Ze PXU, Min L. Wenchuan earthquake and seismic safety of large dams. *J Hydraul Eng* 2008;39:1158–67.
- [2] Wieland M. Concrete face rockfill dams in highly seismic regions. In: Proceedings of the 1st international symposium on Rockfill Dams, Chengdu; 2009.
- [3] Dong WX, Xu WJ, Yu YZ, Lv H. Numerical analysis of earthquake response of an ultra-high earth-rockfill dam. *Nat Hazards Earth Syst Sci Discuss* 2013;1:2319–51. <https://doi.org/10.5194/nhessd-1-2319-2013>.
- [4] Gao L. Performance of dams suffered in Wenchuan earthquake and seismic safety analysis of dams. *J Dalian Univ Technol* 2009;49:657–66.
- [5] Xu B, Zou D, Kong X, Hu Z, Zhou Y. Dynamic damage evaluation on the slabs of the concrete faced rockfill dam with the plastic-damage model. *Comput Geotech* 2015;65:258–65.
- [6] Jiaxuan M, Lixun S. Research on causes of fractures of concrete plates faced on Xibeikou rock-fill dam. *Water Resour Hydropower Eng* 1999;5:012.
- [7] Ke-ming CAO, Yi-sen W, Zhang Z. Design and construction of high concrete face rockfill dam. *Water (Power)* 2001;10:49–52.
- [8] Ying-Zhong YI, Cheng-Yuan WU, Wei MK. Causes and prevention of crack in rockfill dam concrete slab. *Guangxi Water Resources & Hydropower Engineering*; 2006.
- [9] Kong X, Zhou Y, Zou D, Xu B, Yu L. Numerical analysis of dislocations of the face slabs of the Zipingpu concrete faced rockfill dam during the Wenchuan earthquake. *Earthq Eng Vib* 2011;10:581–9. <https://doi.org/10.1007/s11803-011-0091-z>.
- [10] Boulanger RW, Bray JD, Merry SM, Mejia LH. Three-dimensional dynamic response analyses of Cogswell Dam. *Can Geotech J* 1995;32:452–64. <https://doi.org/10.1139/v95-048>.
- [11] Xianxing L, Lihui D. Summary of design of face slab and impervious measures for CFRD. *Water (Power)* 2008;3:012.
- [12] Guoqiang Z, Longshu Z. Application of steel fiber-reinforced concrete in crack resistance of Longshou II hydropower project. *Water (Power)* 2005;30:167–73.
- [13] Yi S, Changcui L, Yunqing W, Jianhua X, Liang L, Quan Y. Design and construction concepts of high concrete facing rockfill dam. *Water (Power)* 2007;8:001.
- [14] Yang Z, Jiang G. Deformation control techniques for 200 m-high Hongjiadu concrete face rockfill dam. *Chin J Geotech Eng* 2008;8:027.
- [15] Qingguo C, Lubing G. Theory and application of steel fiber-reinforced concrete. Beijing: Publishing House of China Railway Industry; 1999. p. 1–7.
- [16] Cheng KH. Fiber reinforced concrete structure. Beijing: Mechanical Industry Press; 2004.
- [17] Wang C. Experimental investigation on behavior of steel fiber-reinforced concrete [M.Sc. thesis]. New Zealand: University of Canterbury; 2006.
- [18] Wen YH, Yang ZY. Researching and exploring of applying concrete with steel fiber in face slab. *Guizhou: Water (Power)*; 2002.
- [19] Ferdinand MG, Budweg S, Dongya. The use of steel fiber-reinforced concrete as the face slab material of concrete face rockfill dam. In: Proceedings of the international symposium on concrete face Rockfill Dam; 2000.
- [20] Lee J, Fenves GL. Plastic-damage model for cyclic loading of concrete structures. *J Eng Mech* 1998;124:892–900. [https://doi.org/10.1061/\(ASCE\)0733-9399\(1998\)124:8\(892\)](https://doi.org/10.1061/(ASCE)0733-9399(1998)124:8(892)).
- [21] Lubliner J, Oliver J, Oller S, Oñate E. A plastic-damage model for concrete. *Int J Solids Struct* 1989;25:299–326. [https://doi.org/10.1016/0020-7683\(89\)90050-4](https://doi.org/10.1016/0020-7683(89)90050-4).
- [22] Pan J, Long Y, Zhang C. Seismic cracking of arch dams and effectiveness of strengthening by reinforcement. *J Hydraul Eng* 2007;38:926–32.
- [23] Pan J, Xu Y, Jin F, Zhang C. A unified approach for long-term behavior and seismic response of AAR-affected concrete dams. *Soil Dyn Earthq Eng* 2014;63:193–202. <https://doi.org/10.1016/j.soildyn.2014.03.018>.
- [24] Pan J, Zhang C, Wang J, Xu Y. Seismic damage-cracking analysis of arch dams using different earthquake input mechanisms. *Sci China Ser E-Technol Sci* 2009;52:518–29. <https://doi.org/10.1007/s11431-008-0303-6>.
- [25] Campione G, Miraglia N, Papia M. Mechanical properties of steel fibre reinforced lightweight concrete with pumice stone or expanded clay aggregates. *Mater Struct* 2001;34:201–10. <https://doi.org/10.1007/BF02480589>.
- [26] Bayramov F, İlki A, Tasdemir C, Tasdemir MA, Yerlikaya M. An optimum design of steel fiber reinforced concretes under cyclic loading. *FraMCos* 2004;5:12–6.
- [27] Maidl B. Stahlfaserbeton. Berlin: Ernst & Sohn; 1991.
- [28] Otter D, Naaman AE. Steel fibre reinforced concrete under static and cyclic compressive loading. *RILEM Symp FRC* 1986;86.
- [29] Zhang Y, Kong X, Zou D, et al. Tensile stress responses of CFRD face slabs during earthquake excitation and mitigation measures. *Int J Geomech* 2017;17(12):04017120.
- [30] Yulu W, Jinbin L, Yan N. Application of autodesk software in earth-rock dam seepage flow computation. In: IOP conference series: materials science and engineering. IOP Publishing, 392(6); 2018. p. 062069.
- [31] Saberi M, Annan CD, Konrad JM. Numerical analysis of concrete faced Rockfill Dams considering the effect of face slab-cushion layer interaction. *Can Geotech J* 2018. [ja].
- [32] Kim YS, Seo MW, Lee CW, et al. Deformation characteristics during construction and after impoundment of the CFRD-type Daegok Dam, Korea. *Eng Geol* 2014;178:1–14.
- [33] Su H, Hu J, Wen Z. Structure analysis for concrete-faced rockfill dams based on information entropy theory and finite element method. *Int J Numer Anal Met* 2012;36(8):1041–55.
- [34] Westergaard HM. Water pressures on dams during earthquakes. *Translator* 1933;98:418–33.
- [35] Xu B, Zou D, Liu H. Three-dimensional simulation of the construction process of the Zipingpu concrete face rockfill dam based on a generalized plasticity model. *Comput Geotech* 2012;43:143–54.
- [36] Liu J, Kong X, Zou D. Effects of interface models on deformation of interface between slab and cushion layer and slab stress of concrete faced rock fill dam. *Chin J Geotech Eng* 2015;37:700–10.

- [37] Lu Y, Liu J. A direct method for analysis of dynamic soil-structure interaction. *China Civil Eng J* 1998;3:008.
- [38] Xu B, Zou D, Liu H. Three-dimensional simulation of the construction process of the Zipingpu concrete face rockfill dam based on a generalized plasticity model. *Comput Geotech* 2012;43:143–54. <https://doi.org/10.1016/j.compgeo.2012.03.002>.
- [39] da Silva AF, de Assis AP, de Farias MM, et al. Three-dimensional analyses of concrete faced rockfill dams: Barra Grande case study. *Electron J Geotech Eng* 2015;20:6407–26.
- [40] Bischoff PH. Tension stiffening and cracking of steel fiber-reinforced concrete. *J Mater Civ Eng* 2003;15:174–82. [https://doi.org/10.1061/\(ASCE\)0899-1561\(2003\)15:2\(174\)](https://doi.org/10.1061/(ASCE)0899-1561(2003)15:2(174)).
- [41] Pastor M, Zienkiewicz OC, Leung KH. Simple model for transient soil loading in earthquake analysis. II. Non-associative models for sands. *Int J Numer Anal Methods Geomech* 1985;9:477–98. <https://doi.org/10.1002/nag.1610090506>.
- [42] Pastor M, Zienkiewicz OC. A generalized plasticity, hierarchical model for sand under monotonic and cyclic loading. In: Proceedings of the 2nd international symposium on numerical models in geomechanics, Ghent; 1986. p. 131–49.
- [43] Xu B, Zhou Y, Zou D. Numerical simulation on slabs dislocation of Zipingpu concrete faced rockfill dam during the Wenchuan earthquake based on a generalized plasticity model. *Sci World J* 2014;2014:572407.
- [44] Zou D, Xu B, Kong X, Liu H, Zhou Y. Numerical simulation of the seismic response of the Zipingpu concrete face rockfill dam during the Wenchuan earthquake based on a generalized plasticity model. *Comput Geotech* 2013;49:111–22. <https://doi.org/10.1016/j.compgeo.2012.10.010>.
- [45] Liu H, Ling HI. Constitutive description of interface behavior including cyclic loading and particle breakage within the framework of critical state Soil mechanics. *Int J Numer Anal Methods Geomech* 2008;32:1495–514. <https://doi.org/10.1002/nag.682>.
- [46] Liu H, Song E, Ling HI. Constitutive modeling of soil-structure interface through the concept of critical state Soil mechanics. *Mech Res Commun* 2006;33:515–31. <https://doi.org/10.1016/j.mechrescom.2006.01.002>.
- [47] Liu J, Zou D, Kong X. A three-dimensional state-dependent model of soil-structure interface for monotonic and cyclic loadings. *Comput Geotech* 2014;61:166–77. <https://doi.org/10.1016/j.compgeo.2014.05.012>.